Carbon Trends 23 (2026) 100623

Contents lists available at ScienceDirect

Carbon Trends

journal homepage: www.elsevier.com/locate/cartre

Flow-induced anisotropy in a carbon black-filled silicone elastomer: Weak structural anisotropy causes strong piezoresistive anisotropy

Bettina Zimmer [a], Bart-Jan Niebuur [a], Florian Schaefer [b], Fabian Coupette [c,d], Victor Tänzel [c,e], Tanja Schilling [c], Tobias Kraus [a,f,*]

[a] INM – Leibniz Institute for New Materials, Campus D2 2, 66123 Saarbrücken, Germany
[b] Materials Science and Methods, Saarland University, Campus D2 3/C5 3, 66123 Saarbruecken, Germany
[c] Institute of Physics, University of Freiburg, Hermann-Herder-Straße 3, 79104 Freiburg, Germany
[d] School of Mathematics, University of Leeds, Leeds LS2 9JT, United Kingdom
[e] Cluster of Excellence livMatS @ FIT – Freiburg Center for Interactive Materials and Bioinspired Technologies, University of Freiburg, Georges-Köhler-Allee 105, D-79110 Freiburg, Germany
[f] Saarland University, Colloid and Interface Chemistry, Campus D2 2, 66123 Saarbrücken, Germany

ARTICLE INFO

Keywords:
Conductive polymer composites
carbon black
Conductive elastomer composites
Shear alignment
piezoresistivty

ABSTRACT

Carbon black (CB)-elastomer composites can serve as low-cost, highly deformable sensor materials. We report on the flow-induced anisotropy of CB-silicone films generated via doctor blade coating. Cured films exhibited larger conductivity perpendicular to the coating direction ($R_{\parallel}/R_{\perp} > 1$). The piezoresistive sensitivity was 2-3 times larger when stretching perpendicular than parallel to the coating direction, with relative resistance increases of 100–200 %. In contrast, the mechanical stress response to strain was isotropic within the measurement uncertainties.

Structural analyses at length scales up to the CB agglomerate level (<1 μ m) yielded only weak structural anisotropy and excluded alignment of small, primary CB aggregates (<150 nm) in flow direction. Small structural anisotropy apparently suffices to induce significant (piezo-)electric anisotropy.

Atomistic molecular dynamics simulations of CB in a viscous medium under strong shear indicate that the CB aggregates have a weak tendency to align with the flow. This generally leads to increased conductivity parallel to the coating $R_{\parallel}/R_{\perp} < 1$. Affine deformation in response to small tensile strain reduces conductivity uniformly.

Our results show that shear can induce the formation of electrically anisotropic composites but excludes shear alignment as dominating mechanism. We propose that anisotropy is caused by an interplay of extensional flow and weak alignment in the flow-vorticity plane that varies under tensile strain.

1. Introduction

Carbon black (CB) is a common filler material used to tune mechanical properties of rubbers [1–5]. In addition, it introduces electrical conductivity when its concentration exceeds a critical value (percolation threshold) needed to form a network within the polymeric matrix [6–9]. CB-filled elastomers can thus be used to create flexible electrodes and highly deformable piezoresistive sensors [3,10–14]. Compared to conductive fillers like carbon nanotubes (CNTs) [15–17], graphene [18,19], and silver nanoparticles [20,21], CB is an attractive alternative in that it is less expensive and more readily available [1].

To optimize CB elastomers for electronic applications, the correlation between structure, the distribution of CB and its agglomerate structure, and electromechanical properties must be understood. Literature on CB composites reports on numerous relevant factors, e.g., CB primary structure and surface chemistry [4,22–24], CB aggregate size distribution [25,26], CB-matrix interactions [27], additives (e.g. ionic liquids [28,29], inorganic salts [26], non-ionic plasticizer [30]), matrix viscosity during processing [31], and curing temperature [31]. Processing has a decisive impact on the CB distribution and the electromechancical properties [1–3,6,7,32–36]. Depending on the flow history of the precursor (mixture of CB and the still liquid matrix), different CB morphologies can form, including anisotropic ones. These anisotropic structures are associated with material flow in preferential directions as experienced during injection molding [35], compression molding [2,6], melt-casting [37], and extrusion [36].

* Corresponding author at: INM – Leibniz Institute for New Materials, Campus D2 2, 66123 Saarbrücken, Germany.
E-mail address: tobias.kraus@leibniz-inm.de (T. Kraus).

https://doi.org/10.1016/j.cartre.2026.100623
Received 22 October 2025; Received in revised form 29 January 2026; Accepted 7 February 2026
Available online 11 February 2026

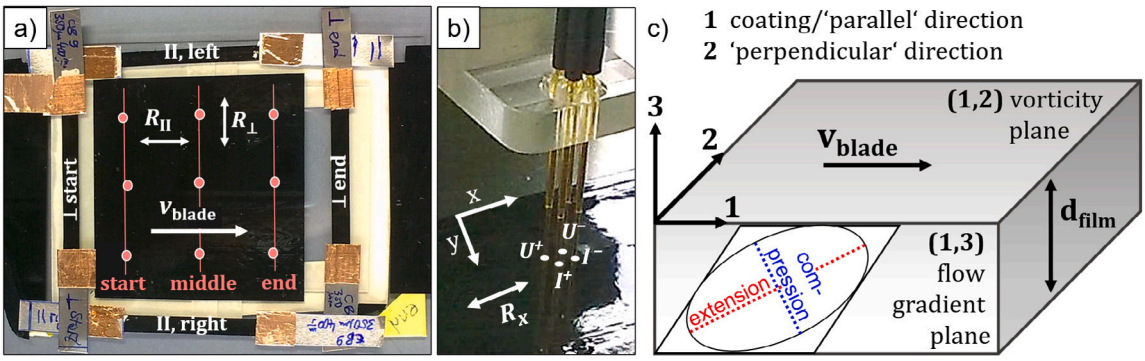

Fig. 1. Directions and planes relevant for characterizing the CB-silicone films. (a) Film with tensile specimens cut from near the edges and example of measuring grid (spacing 3–4 cm) for electrical four-point measurements indicating 'start', 'middle', and 'end' positions, (b) probe arrangement and polarity of four-point measurements in the square setup, (c) definition of directions and planes with respect to the coating direction.

In this study, we focus on anisotropy in CB-filled elastomers and discuss which structures are affected by liquid motion during production. Flow affects the material's piezoresistivity, the strain-induced resistance changes that are exploited in sensors. While extensive research on flow-induced anisotropy has been done on CB suspended in low viscosity organic liquids [38–41] and CB-filled thermoplasts [6, 35–37], literature on the microstructure-dependent electromechanical properties of CB elastomers is scarce. We did not find any work for CB elastomers with chemically crosslinked matrices (e.g. silicone rubber) and only two publications [2,37] for CB-filled thermoplastic elastomers (thermoplastic matrix with elastomeric properties). Flandin et al. [2] briefly discussed the possible role of compression molding in the electrical anisotropy of a CB-filled ethylene-octene elastomer in the undeformed state. However, as no structural analyses were performed, the structure–property relationship remained unclear. Ehrburger-Dolle et al. [37] reported anisotropic X-ray scattering patterns of ethylene propylene rubber with CB contents slightly above the percolation threshold. The anisotropy, which presumably originates from the liquid composite being sheared during melt-casting, is correlated with different degrees of interpenetration of CB aggregates in two principal orientations.

The publications discussed above provide no link between the principal orientations in the anisotropic patterns that filler particles formed and the flow conditions. The authors did not analyze the consequences for electrical conductivity. Here, we choose an experimentally well-accessible system based on a silicone with a liquid precursor that can be thermally cross-linked. We thus avoid complex effects of temperature differences in the polymer melt. This allowed us to use doctor blading and thus modulate shear via slit size and blade velocity. A standard CB was used at different volume fractions. This resulted in composites similar in structure and conductivity to widely applied carbon-filled rubbers.

To explore flow-induced anisotropy in CB elastomers, we incorporated CB in a thermosetting silicone matrix and exposed the liquid mixtures to shear flow by means of doctor blade coating at two gap heights (60 µm, 350 µm) and various coating speeds. The resulting films were cured at elevated temperature to retain the process-induced microstructure. Electrical resistances of cured, unstrained films of three CB concentrations above the percolation threshold were measured both parallel and perpendicular to the coating direction. The influence of process parameters such as coating speed and film thickness was investigated (Section 3.1). In addition, piezoresistivity was studied via uniaxial tensile tests with in-situ electrical resistance measurement along the stretch axis (parallel or perpendicular to the coating direction, Section 3.2).

The shear that the doctor blade exerted on the uncured CB-silicone mixtures led to significant electrical and piezoresistive anisotropy in the cured material, whereas mechanical anisotropy was negligible. We discuss implications of this (piezo-)electric anisotropy for industrial practice and explore its structural origin via characterization of unstretched and stretched states by small-angle X-ray scattering (SAXS), as well as nanomechanical mapping (PeakForce QNM) combined with segmentation of the signal maps (Section 3.3). In addition, we present simulations of the fractal filler network, focusing on the impact of shear flow on particle alignment and consequences for electrical anisotropy (Section 3.4). Ultimately, we formulate a hypothesis describing the structural processes that explain the observed phenomenology (Section 3.5).

2. Experimental

2.1. Film fabrication and sample preparation

CB-filled elastomeric films of at least $5 \times 7\,cm^2$ were prepared in ambient air by dispersing CB (acetylene, 100% compressed, 99.9+%, Thermo Scientific Chemicals) at 7/9/11 vol% CB (above the percolation threshold of ~5 vol% [25]) in a crosslinking silicone matrix (Sylgard® 184, Dow®), doctor blade coating the resulting reactive mixtures (two gap heights, h_{gap} = 60 µm and 350 µm), and curing for 2 h at 100 °C. In order to assess the impact of dynamic effects during processing on final properties, the blade speed, v_{blade}, was varied between 5 mm/s and 400 mm/s. The resulting global shear rates ($\gamma_{global} = v_{blade}/h_{gap}$) span a large interval of $60\,s^{-1}$ to $3300\,s^{-1}$. More details on film fabrication are provided in Appendix A.

Cured, unstrained films were characterized electrically by the four-point method (Section 2.2.1) without any further sample preparation. Samples for tensile test with in situ electrical two-point measurement, PeakForce QNM and SAXS, were coated at h_{gap} = 350 µm, 20 mm/s. We cut pieces for characterization from near the edges of the films as exemplified in Fig. 1a (left/right side for stretch parallel to the coating direction, start/end position for stretch perpendicular to the coating direction). Exact sample dimensions are given in the corresponding sections (2.2.2, 2.2.3 and 2.2.4).

2.2. Characterization

2.2.1. Four-point probe measurement

To quantify electrical anisotropy in undeformed films, electrical resistance was measured parallel and perpendicular to the coating direction, using a Keithley instrument (2450 Interactive SourceMeter®, current sweep from −10 µA to +10 µA, R obtained from linear fits of the ohmic voltage-current curves) with a customized four-point probe setup in the square arrangement (Fig. 1b), in ambient air (22 ± 1 °C, 26 ± 19% r.h.). With the used probe distance of 2 mm, all films can be

Table 1
Film thicknesses of samples used in uniaxial tensile testing with electrical resistance measurements.

Parallel to coating direction:		
Carbon volume fraction	Thickness [µm]	Standard deviation [µm]
0%	267	12
0%	264	16
7%	268	9
7%	278	9
9%	301	2
9%	306	2
11%	345	17
11%	330	8
Normal to coating direction:		
Carbon volume fraction	Thickness [µm]	Standard deviation [µm]
0%	280	28
0%	262	25
7%	293	12
7%	262	3
9%	324	10
9%	267	18
11%	319	20
11%	328	46

approximated as thin films. Resistance R in parallel ($\parallel$) and orthogonal to the coating direction ($\perp$) can be expressed as [42]

$$R_{\parallel} = \frac{\sqrt{\rho_{\parallel}\rho_{\perp}}}{2\pi \cdot d_{\text{film}}} \cdot \ln(1 + \rho_{\parallel}/\rho_{\perp}) \tag{1}$$

$$R_{\perp} = \frac{\sqrt{\rho_{\parallel}\rho_{\perp}}}{2\pi \cdot d_{\text{film}}} \cdot \ln(1 + \rho_{\perp}/\rho_{\parallel}) \tag{2}$$

with the intrinsic resistivities in the $\parallel$- and $\perp$-directions, ρ_x and ρ_y, and the film thickness d_{film}.

Spatial variations were analyzed by choosing three or four measuring spots at the 'start', 'middle' and 'end' sections (referring to the coating direction) of each film, as schematically depicted in Fig. 1a. The respective mean and maximal error of $R_{\parallel}$ and $R_{\perp}$ over all spots per section (one measurement per spot for each orientation) were calculated.

The quotient of resistances measured in both directions quantifies electrical anisotropy and grows monotonically with the ratio of the intrinsic resistivities [42]:

$$\kappa := \frac{R_{\parallel}}{R_{\perp}} = \frac{\ln(1 + \rho_{\parallel}/\rho_{\perp})}{\ln(1 + \rho_{\parallel}/\rho_{\perp})} \,. \tag{3}$$

We refer to $R_{\parallel}/R_{\perp}$ as "electrical anisotropy ratio" in the following.

2.2.2. Uniaxial tensile test with electrical two-point probe measurement

To study piezoresistivity, uniaxial tensile tests (universal testing machine Zwick 1446) with in-situ electrical two-point measurements (DAQ6510 by Keithley, constant test current of 10 µA in 'auto range' mode) were performed in ambient air (22 ± 1°C, 30 ± 15% r.h.). Rectangular strips of $4 \times 55\,\text{mm}^2$ were cut from 'thick' films ($h_{\text{gap}} = 350\,\mu\text{m}$), coated at 20 mm/s, and stretched either parallel (engineering strain $\epsilon_{\parallel}$) or perpendicular ($\epsilon_{\perp}$) to the coating direction (cf. Fig. 1a). The film thicknesses of the different samples are summarized in Table 1.

For in-situ resistance measurement along the respective stretch axis, $R_{\parallel}(\epsilon_{\parallel})$ and $R_{\perp}(\epsilon_{\perp})$, aluminum strips were glued to the top and bottom of the samples with conductive silver glue and fixated with copper foil. The resulting probe distance is identical to the gauge length for straining and equaled $L_0 = 35$ mm in the relaxed state.

After mounting, the tensile force was zeroed and the sample stretched to a pre-load of 0.05 N. The tensile test started after both force and electrical resistance had stabilized (roughly after 20–25 min), with the force zeroed at the start of the loading phase. The testing procedure consisted of 4 load-unload cycles between 0% strain and maximal strains of $\epsilon_{\text{max}} = 10/20/30/40\%$, with a strain rate of $10^{-2}\,\text{s}^{-1}$ (controlled via the position of the crosshead). After each loading and unloading, the material was allowed to relax for 20 min at the given strain plateau. Resistance values for each strain plateau were inferred from the relaxation process as explained in Appendix B.

To distinguish the effect of doctor blade coating on the CB network from the impact on the silicone matrix, neat Sylgard (cf. Appendix A) was characterized in addition to the CB composites (7/9/11 vol% CB). Mechanical testing was identical to the CB-filled samples except for a lower pre-load (0.02 N) since the unfilled material is much less stiff.

Resistance measured along a stretch axis R_i is proportional to the intrinsic electrical resistivity ρ_i

$$R_i(\epsilon_i) = \rho_i(\epsilon_i) L(\epsilon_i)/A(\epsilon_i) \tag{4}$$

with the sample length L and cross-sectional area A. Both electrical and mechanical anisotropy can cause piezoresistive anisotropy.

2.2.3. Nanomechanical mapping of filler distribution

Nanomechanical mapping was done on the sample surface (vorticity plane, see Fig. 1) to probe the dispersion state of near-surface CB aggregates and agglomerates, using Bruker's SFM mode PeakForce QNM™. It outputs sample topography ('height' signal) as well as local material properties (cf. Appendix D1 for explanation and [43–45] for details). A detailed methodological discussion of the performed measurements is given in Appendix D2.

Unstrained and strained ($\epsilon_i = 40\%$) samples of 350 µm-films coated at 20 mm/s were characterized (cf. Section 2.1). Probe and measuring parameters were chosen to give clean force-distance curves on the soft areas dominated by the silicone matrix as well as on the much stiffer CB-rich regions. Regions dominated by CB are much less deformable than the ones dominated by the silicone matrix, with indentation depths of a few nm to about 20 nm. The resulting lateral resolution suffices to discriminate CB aggregates as our results (cf. 3.3.1) illustrate.

Image segmentation for analysis of CB particles was carried out with ImageJ [46] and Fiji 2.15.8 [47]. The procedure is explained in detail in Appendix D2. The dissipation signals of the PeakForce QNM measurements were first converted into 8-bit grayscale images using Gwyddion (2.64, Delayed Drifter). The images were then segmented using numerical gray value thresholding, as shown in Fig. D.3d. The threshold was set using the device-internal *MaxEntropy* algorithm.

The volume fraction η_V of the CB particles was estimated through the area fraction η_A, i.e. the fraction of particles in a perfect two-dimensional surface section through the bulk sample [48], assuming a uniform density of CB particles in the film. Individual particles were detected, and their alignment was quantified by obtaining the angle at which the Feret diameter was maximal. Particle size and circularity distributions were inferred from the cross-sectional area of the particles (cf. Fig. 6 in Section 3).

2.2.4. Small-angle X-ray scattering

SAXS measurements were performed on a laboratory-scale Xeuss 2.0 instrument (Xenocs SA, Grenoble, France). The X-ray beam from a copper K_α source (wavelength 1.54 Å) was focused on the sample with a spot size of $0.25\,\text{mm}^2$. The samples were located at a sample-detector distance (SDD) of 2500 mm, calibrated using a silver behenate standard. The resulting measurable momentum transfer, q, ranges from $0.005\,\text{Å}^{-1}$ to $0.2\,\text{Å}^{-1}$, with q being defined as $q = 4\pi \sin(\theta/2)/\lambda$ and θ the scattering angle. Two-dimensional scattering patterns were obtained using a Pilatus 300K detector (Dectris, Baden, Switzerland) with a pixel size of $0.172 \times 0.172\,\text{mm}^2$ and an acquisition time of 1 h for each sample.

The samples (0 vol% CB coated at 400 µm, 20 mm/s and 9 vol% CB coated at 350 µm, 20 mm/s, ~$7 \times 50\,\text{mm}^2$-strips cut from near the film edges parallel and perpendicular to the coating direction, respectively) were placed directly in the beam without a sample container. Sample strain is induced by manually stretching and fixing the samples at 140% of their original length (nominal strain of 40%). To obtain $I(q)$ parallel

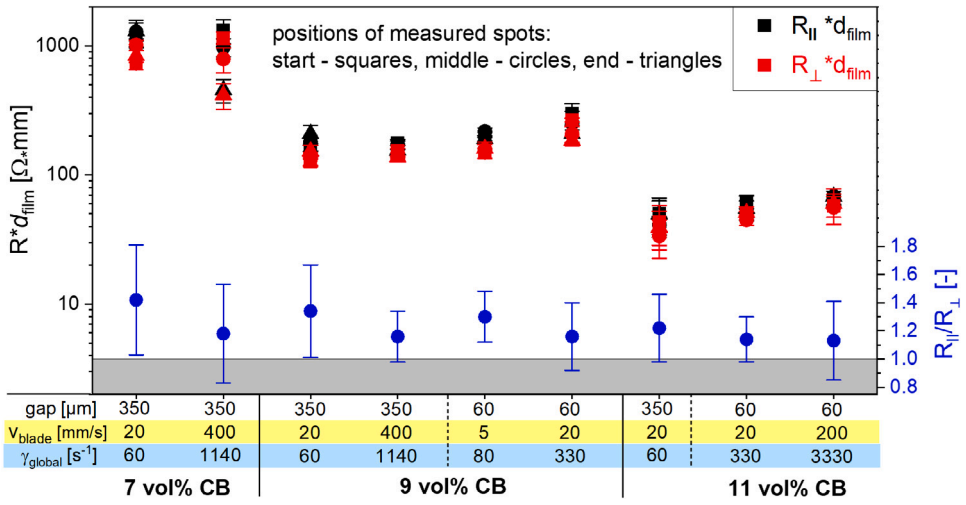

Fig. 2. Electrical resistances of CB-silicone films (7/9/11 vol% CB, gaps 60/350 µm, blade speeds 5–400 mm/s) measured parallel and perpendicular to the coating direction, $R_{\parallel}$ and $R_{\perp}$ (multiplied by film thickness to compensate geometric variations, see Eq. (1) in Section 2.2.1), at the start, middle and end position of the films (mean and maximal error from 3–4 points on each position), and resulting anisotropy ratio, $R_{\parallel}/R_{\perp}$. The mean and maximal error of $R_{\parallel}/R_{\perp}$ were calculated from all local pairs of $R_{\parallel}$ and $R_{\perp}$ of a given film (9–12 measuring spots, see Section 2.2.1 for visualization of the measuring grid).

and perpendicular to the direction of strain, the 2D scattering patterns were azimuthally averaged within two angle ranges subtending 20° parallel and perpendicular to the direction of strain, respectively.

The scattering curves of the unloaded silicon films were fitted to an ansatz comprising three separate contributions

$$I(q) = I_{LS}(q) + I_{fluct}(q) + I_0 \,. \tag{5}$$

Scattering by the large scale structures is captured by a generalized Porod law

$$I_{LS}(q) = \frac{K_P}{q^m} \tag{6}$$

with Porod amplitude K_P and Porod exponent m. The Ornstein-Zernike structure factor accounts for scattering by composition fluctuations on the level of single chains

$$I_{fluct}(q) = \frac{I_{OZ}}{1 + \xi^2 q^2} \tag{7}$$

with the Ornstein-Zernike amplitude I_{OZ} and the correlation length ξ of composition fluctuations [49,50]. I_0 is a constant background. R^2 values in the range of 0.986–0.997 were obtained, indicating an excellent agreement between the measured data and the fitted model for all measurements.

3. Results and discussion

3.1. Electrical anisotropy of unstrained films

Electrical resistances of unstrained films in the two main orientations relative to the coating direction, $R_{\parallel}$ and $R_{\perp}$, along with corresponding values of the electrical anisotropy ratio κ are illustrated in Fig. 2. Resistance values are scaled by the corresponding film thickness to eliminate geometrical effects and facilitate comparison (see Eq. (1) in Section 2.2.1). Symbols indicate the start, middle and end sections of film coatings. We found no relevant variation of resistances along the coating direction with one exception (7 vol% CB, 400 mm/s) where the end positions display significantly lower resistances, both parallel and perpendicular to the coating direction.

Resistance values parallel to the coating direction were systematically higher than perpendicular to it. All films exhibit an electrical anisotropy ratio κ between 1.1 and 1.4. Thus, doctor blade coating of the uncured CB-silicone mixtures introduced electrical anisotropy. Within experimental error, the degree of electrical anisotropy depended neither on CB concentration nor on film thickness or blade speed. This is surprising as all these parameters have a big impact on hydrodynamic properties of the sample: Increasing CB content from 7 vol% to 11 vol% leads to much more viscous mixtures, evident during the coating process, and the variations of film thickness and blade speed imply a large range of global shear rates of approximately $50 - 3080\ s^{-1}$ (see Fig. 2).

Flow-induced electrical anisotropy in carbon filler-polymer composites has been reported previously. For example, CB-filled thermoplasts [6,35,36] and a CNT-filled silicone [51] all exhibited larger electrical conductivity in the direction of melt flow compared to the perpendicular direction. This was explained by preferential alignment within the composite. Yet, in [35,36], the alignment refers to the polymer chain segments rather than to CB. Electrical anisotropy originated from an anisotropic spatial distribution of CB particles rather than a preferential orientation of individual aggregates or agglomerates. The inhomogeneous distribution of CB was induced by packing and orientation of the matrix chains during processing, for instance, by CB adsorption to aligned PET fibers [36]. Therefore, flow-induced anisotropy is generally not equivalent to alignment of filler particles along the shearing direction.

In fact, work on low molecular weight CB suspensions report anisotropic CB structures aligned perpendicular to the shearing direction [38–41,52]. In any case, larger conductivity perpendicular to the shear direction is unusual and yet to be explained. The underlying mechanism shows similar efficiency across the given range of flow kinetics and shear forces. Even the lowest shear rate of $50\ s^{-1}$ is sufficient to induce anisotropy. This is consistent with the fragmentation of a weak network of CB agglomerates upon exceeding a critical shear rate which typically leads to shear-thinning behavior [53,54]. Since the latter has been reported for a mixture very similar to our uncured CB-silicone mixtures in the concerned range of shear rates (see [28]), we propose that the CB network gets disrupted by the shear forces, becomes anisotropic as a result of shear flow, and reforms rapidly upon cessation of shear. In the following sections we gather additional experimental evidence for this structural picture and ultimately discuss all findings together in Section 3.5.

3.2. Piezoresistive anisotropy

We now consider how flow-induced anisotropy affects piezoresistivity, i.e., strain-induced resistance changes. For this, we compare the electrical resistance and mechanical stress in response to uniaxial strain

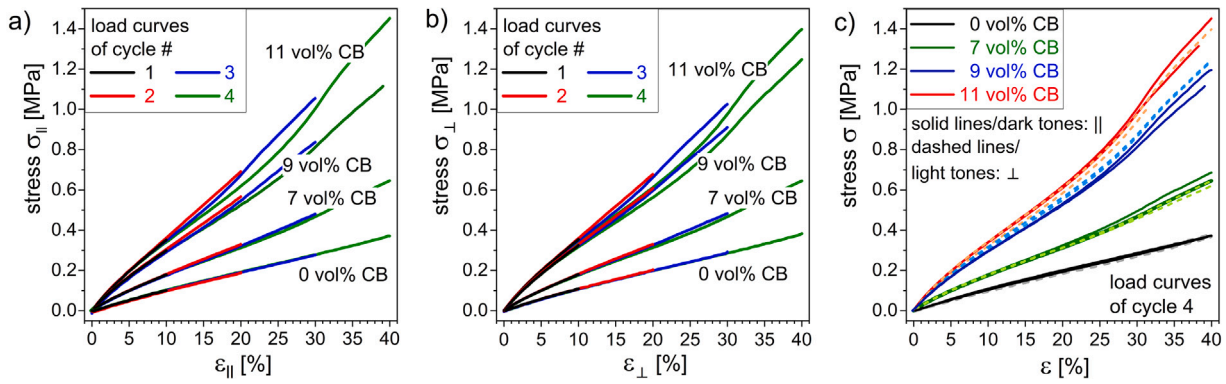

Fig. 3. Stress responses of CB-silicone films to uniaxial strain (strain rate $10^{-2}\,s^{-1}$, $22 \pm 1\,°C$, $30 \pm 15\%$ r.h.). Stress–strain curves (nominal stress, σ, vs. nominal strain, ϵ) of: (a) all load cycles for stretch parallel to the coating direction, (b) all load cycles for stretch perpendicular to the coating direction, (c) load phase of cycle 4 for all samples and stretching directions.

measured parallel and perpendicular to the coating direction. Since mechanical anisotropy can lead to piezoresistive anisotropy (see eq. (4) in Section 2.2.2), we first discuss the mechanical stress response to strain (Section 3.2.1) before examining the piezoresistive sensitivity (Section 3.2.2).

3.2.1. Mechanical anisotropy

Fig. 3 shows the mechanical stress in response to strain across a variety of samples. The stress–strain curves get steeper with increasing CB concentration, i.e., CB reinforced the composites. This is indicative of strong filler-matrix adhesion and a fine dispersion of CB in the matrix and confirmed by nanomechanical mapping (see Section 3.3.1). Furthermore, the load cycles for CB-filled silicone indicate strain softening. The composites became less stiff with increasing cycle number (evident for ≥10% strain), and the effect was stronger for higher CB contents (maximal for 11 vol% CB, stress reduction by up to ∼15%). This is common in filled rubbers and referred to as the Mullins effect [55].

The tensile tests brought no signs of mechanical anisotropy whatsoever; it is conceivable that such anisotropy exists but it was too weak to differentiate from the scatter, and much smaller than the electrical anisotropy. Fig. 3a–c illustrates the same stress response for the two stretch axes, $\sigma_{\parallel}(\epsilon_{\parallel})$ and $\sigma_{\perp}(\epsilon_{\perp})$, within experimental scatter of $3-5\%$. In contrast, electrical conductivity was clearly anisotropic, both in the unstrained (Section 3.1) and strained state (Section 3.2.2). We conclude that the structural mechanism responsible for electrical anisotropy is either irrelevant for the mechanical stress response or its mechanical effect too weak to be resolved.

3.2.2. Anisotropy of piezoresistive sensitivity

As Fig. 4 illustrates, electrical resistances always increased when applying uniaxial strain parallel or perpendicular to the coating direction, respectively. As exemplified by the data for 9 vol% CB (Fig. 4a), the resistance increase is much more pronounced for stretch perpendicular to the coating direction. Accordingly, piezoresistive sensitivity is higher perpendicular to the coating direction ($\mathrm{d}R_{\perp}(\epsilon_{\perp})/\mathrm{d}\epsilon_{\perp} > \mathrm{d}R_{\parallel}(\epsilon_{\parallel})/\mathrm{d}\epsilon_{\parallel}$).

Resistance increased monotonically with strain (Fig. 4b–d). A strain-induced increase in resistivity is common for such composites at small to moderate stretches up to 30% [2,10,11,36,56] and attributed to growing CB interparticle distances [8,11,13,36,56]. The mechanical isotropy suggests that the geometrical contribution to $R(\epsilon)$ is irrelevant for piezoresistive anisotropy, i.e., the latter is solely based on anisotropic changes in intrinsic resistivity.

Fig. 4b–e displays the irreversible and reversible resistance increases that we measured. The irreversible part grew roughly linear with strain. The irreversible resistance increase is commonly attributed to damage to the filler-matrix interphases [8,56,57]. The isotropic strain-softening observed mechanically corroborates this idea. The irreversible part of the resistance increase is likewise indifferent to the coating direction. Consequently, the structural process driving piezoresistive anisotropy is reversible.

The anisotropy in piezoresistive sensitivity (Fig. 4f) was significantly stronger than the mechanical anisotropy with relative resistance increases of about 100 to 200 %. Electrical properties of the composite are thus much more strongly affected by flow-induced anisotropy than mechanical properties. Electrical conductivity requires a percolating network of tunneling contacts between CB particles, whereas mechanical reinforcement does not. Close to the percolation threshold (≈5 vol% [28]) we hence expect resistances to be more sensitive to any external perturbation [3,4,8,11]. The measurements meet this expectation, i.e. all strain induced resistance changes become less pronounced for large carbon content. The same also applies for the electric anisotropy (cf. Fig. 4f).

An increase in flow-induced anisotropy has been previously reported for the electrical conductivity of CB thermoplasts [6,36] and magnetically aligned graphite fibers in an epoxy [58], and has been studied using X-ray scattering of the CB network in ethylene propylene rubber [37]. Structural models of anisometric conductive particles aligned in a dielectric continuum predict that the largest anisotropy occurs close to percolation [58]. It is likely that the same basic model holds true for our composites. We analyze below whether similar alignment of anisotropic CB particles or superstructures causes the anisotropy of piezoresistance in our composites.

In summary, the electrical anisotropy from shear flow during film fabrication in our composites was weak ($R_{\parallel}/R_{\perp} = 1.1 - 1.4$) in the undeformed state, but strong upon deformation as a result of anisotropic piezoresistive sensitivities.

For CB concentrations well above the percolation threshold anisotropy in piezoelectric sensitivity is less pronounced. More details on the anisotropic sensing performance of our CB-silicone films are discussed in Appendix C.

3.3. Structural analysis

3.3.1. Nanomechanical anisotropy mapping

We used a nanomechanical probe technique to analyze the distribution of and detect anisometry at the level of CB aggregates. The $20 \times 20\,\mu m^2$ PeakForce QNM dissipation maps of unstretched samples shown in Fig. 5a–c reflect the dispersion CB distribution near the surface. We found that CB was well-dispersed in the matrix for all compositions with agglomerates of a few 100 nm, see Fig. 5d–e. Such fine dispersions are known to form reinforcing CB-matrix interphases [59], explaining the mechanical effect of CB. We found few larger agglomerates (Fig. 5, Fig. D.2), and none with diameters above 1 μm.

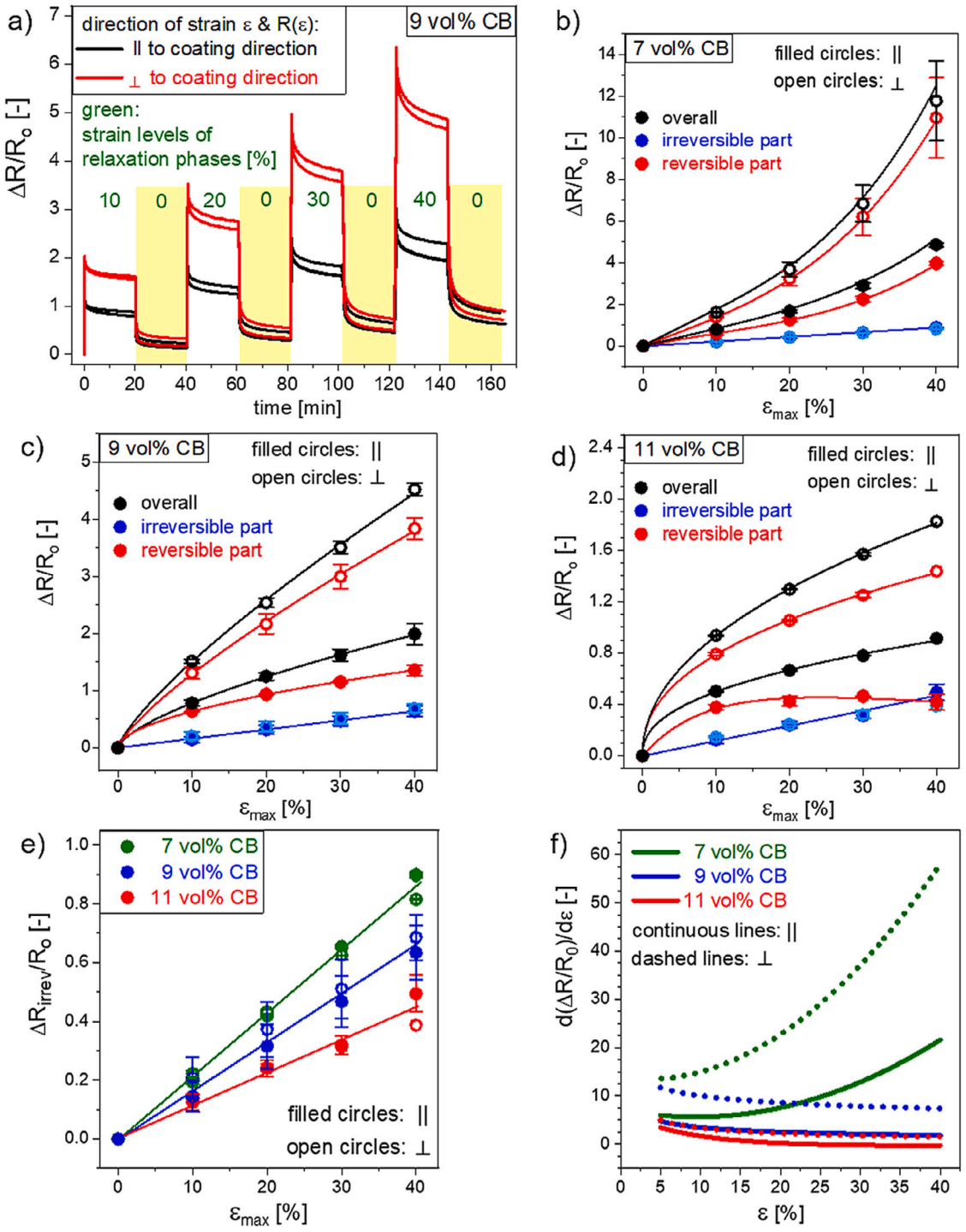

Fig. 4. Electrical resistance response of CB-silicone films to uniaxial strain parallel and perpendicular to the coating direction, respectively. (a) Example of resistance change relative to initial value before stretching, R_0, during load-unload cycles (9 vol% CB, to ϵ_{max} = 0/10/20/30/40%, 22 ± 1 °C, 30 ± 15% r.h.), (b–d) overall relaxed resistance change relative to R_0 (mean and maximal error from two samples each), along with irreversible (permanent increase after unloading) and reversible (overall minus irreversible increase) parts (lines = guide to the eye), (e) irreversible parts (lines = trend as guide to the eye), (f) first derivatives of lines in panels b–d as a measure of piezoresistive sensitivity.

We obtained 5 × 5 µm² maps (see Fig. 5d–f for a selection) of unstrained and strained samples of the 7 vol% CB film (strongest piezoresistive anisotropy) to detect structural anisotropy. A significant portion of CB aggregates (visible as coherent dark spots) and agglomerates (clusters of aggregates separated by thin yellowish lines in the maps) was anisometric, but we did not observe clear trends on preferential alignment. For example, the maps for the sample strained parallel to the coating direction give an ambivalent picture: In some regions, aggregates appear preferentially oriented along the axis of coating/stretching (left part of Fig. 5e), while they tend to be aligned perpendicular to the axis in other regions (right part of Fig. 5e).

We used automatic segmentation to analyze statistically significant numbers of particles. The 10 × 10 µm² dissipation maps were segmented and evaluated for zero strain and 40% strain parallel and perpendicular to the coating direction (cf. experimental method, Section 2.2.3 and Fig.

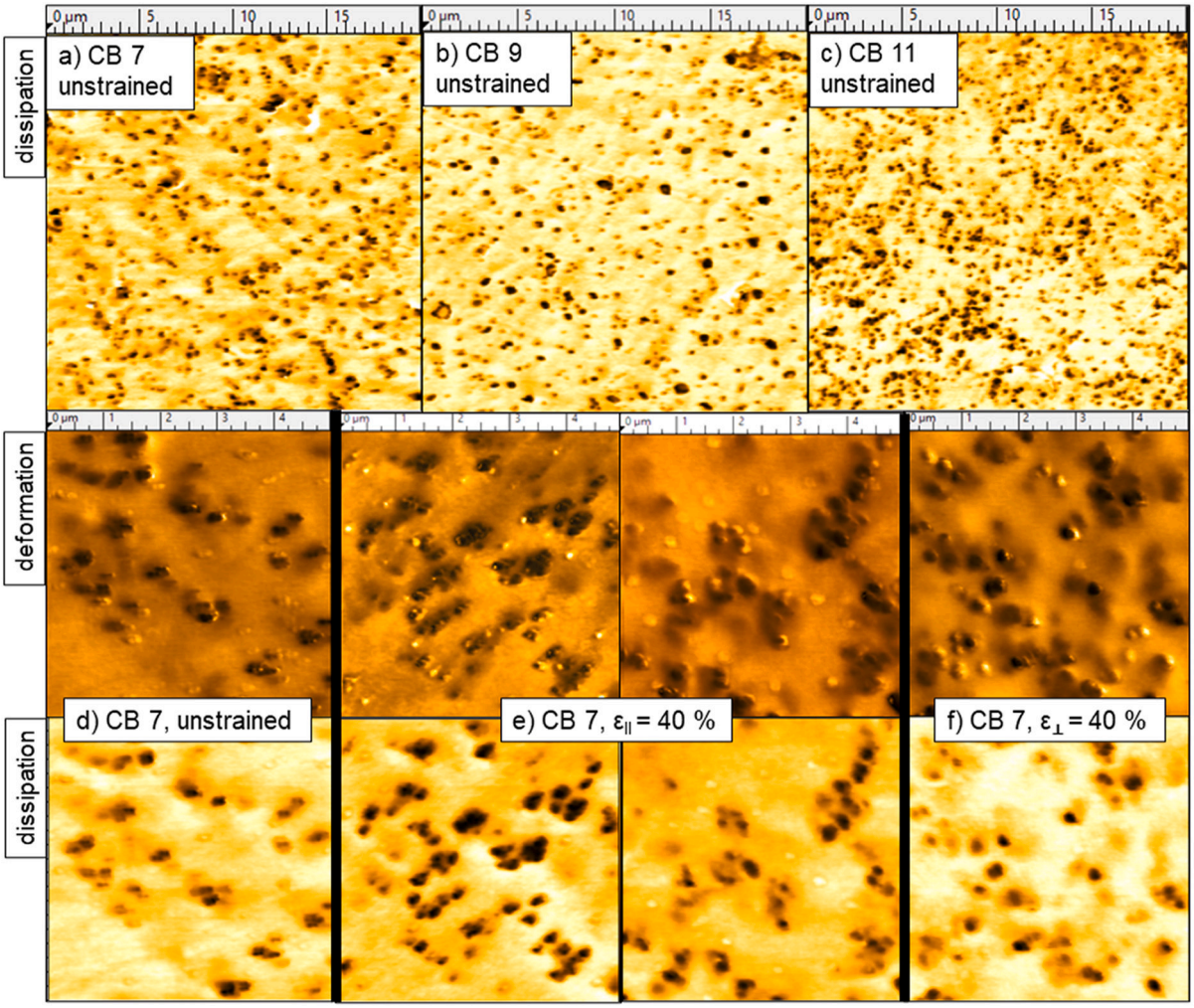

Fig. 5. PeakForce QNM maps mirroring the near-surface CB morphology of CB-silicone films. (a–c) $20 \times 20\,\mu m^2$ dissipation maps of unstretched films with 7/9/11 vol% CB, (d–f) $5 \times 5\,\mu m^2$ deformation and dissipation maps of 7 vol% CB samples in the unstrained state vs. strained, relaxed states at $\epsilon_{\parallel} = 40\%$ and $\epsilon_{\perp} = 40\%$, respectively. In each of the maps, the coating direction goes from bottom left to top right.

D.4). Fig. 6 shows the resulting histograms and average values of the particle diameter, circularity as well as the angle of the major Feret axis to the horizontal direction.

CB particle diameters roughly followed a log-normal distribution and agreed with visual results and aggregate sizes measured in toluene [25]. Circularities were monomodially distributed with the maximum ranging between 0.75 and 0.85 and tailing towards small circularities. This indicates slight anisometry on average with few large outliers akin to the size distribution. The Feret angles for the unstrained films revealed two maxima at approximately 20° and 170° relative to the horizontal (scanning) direction. Neither of the two modes align well with coating or perpendicular direction at 45° or 135°, respectively. Yet, the distribution is evidently different from uniform. Thus, there seems to be some degree of diffuse aggregate alignment in the flow-vorticity plane which appears largely indifferent to the external strain. In summary, structural anisotropy likely exists in the composite, but there is no indication of strong alignment with any of the distinguished axes of symmetry.

3.3.2. Structural anisotropy analysis with X-ray scattering

Small-angle X-ray scattering (SAXS) measurements were performed to study the bulk structure of unstretched and stretched silicone films, both neat and filled with CB at a concentration of 9 vol%. Fig. 7a presents one-dimensional scattering patterns of the neat silicone film in its unstretched state, obtained by azimuthally averaging the two-dimensional scattering patterns in a narrow angular range, both in the coating direction and perpendicular to it (see experimental section for more information). Both curves feature a shoulder at $\sim 0.04\,\text{Å}^{-1}$, assigned to scattering at composition fluctuations within the silicone network. With Eq. (5), the correlation length of composition fluctuations, ξ, is found proportional to the mesh size of the silicone network. Its values of 2.43 ± 0.03 nm parallel and 2.22 ± 0.03 nm perpendicular to the coating direction indicate structural anisotropy of the silicone matrix. This anisotropy presumably stems from extensional flow of chain segments in the parallel direction during coating of the still liquid silicone.

Strain increased the mesh size in the direction of strain and reduced it normal to it (Fig. 7b, c), reflecting transverse contraction. The Poisson ratios according to Hencky, $\nu = -\ln(\lambda_{trans})/\ln(\lambda_{axial})$, were $\nu_{\parallel} = 0.45 \pm 0.09$ parallel and $\nu_{\perp} = 0.44 \pm 0.11$ normal to the coating direction, indicating the nearly incompressible behavior typical of rubbers and consistent with the results of Section 3.2.1. The small directional differences in crosslink density are apparently too weak to resolve.

The scattering of silicones filled with 9 vol% CB (Fig. 7d) showed a steep slope in the entire measured q range, indicating that CB particles and their agglomerates were present at all length scales. Scattering patterns were identical parallel and perpendicular to the coating direction. This remained true when stretching the composite parallel

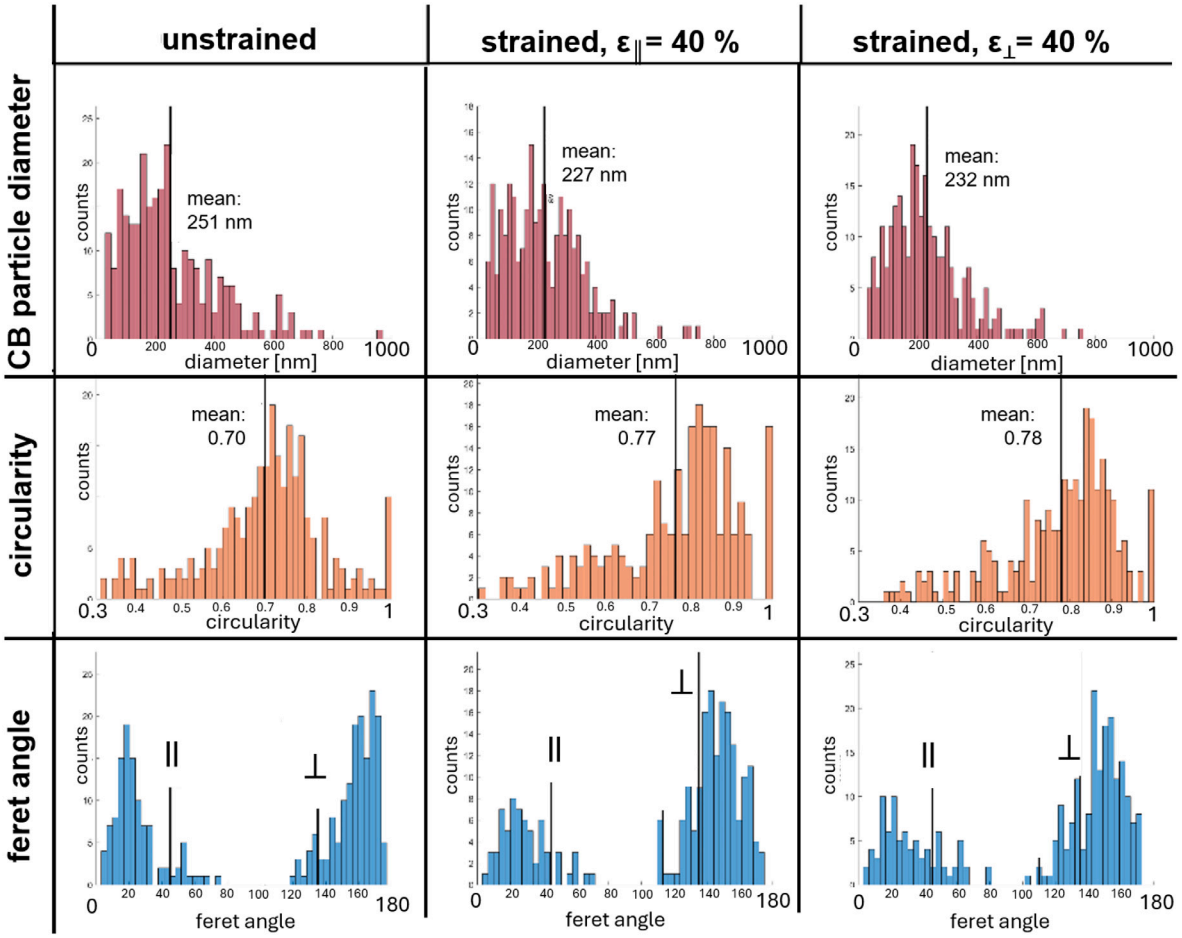

Fig. 6. Assessment of CB particle diameter, circularity and angle of the major Feret axis to the horizontal axis of the PeakForce QNM scans by histograms obtained from segmentation analysis of $10 \times 10\,\mu m^2$ dissipation maps.

(Fig. 7e) and perpendicular (Fig. 7f) to the coating direction. We conclude that neither coating nor straining introduced structural anisotropy at length scales between ~1 nm and ~150 nm, i.e., small CB aggregates of only a few primary particles (diameters of approximately 40 nm [25]) were not aligned with either of the distinguished axes. Structural anisotropy in the CB network may exist at larger length scales, different angles, or it may simply be too weak resolve. In particular, interparticle distances may be larger in the parallel direction, analogous to the mesh size anisotropy of the silicone matrix reported above, as a result of extensional flow which pulls apart CB aggregates and agglomerates.

The analyses above indicate that only weak structural anisotropy exists at the nano- and micrometer scales. In the following, we use simulations to rationalize these results and to understand why shear alignment is weak, and how weak structural anisotropy can lead to the piezoresistive anisotropy that we observed.

3.4. Simulations

We used simulations inspired by previous computational studies [60] and experiments [61] on the alignment of filler particles in a simple shear flow. Stiff CB aggregates [25] were the fundamental building blocks of our simulation. In the following description of our simulations we focus on the relevant conceptual aspects. More detail and explicit parameter choices can be found in appendix E. Our aggregates consist of primary spheres of diameter σ that are rigidly fused together in the course of a diffusion limited aggregation (DLA) process. As a consequence, aggregates are Brownian trees exhibiting a power-law decaying density profile which corresponds to a fractal dimension of $d_f \approx 2.5$, similar to experimentally observed fractal dimensions of certain CB varieties (cf. [62]). The tenuous agglomerate structures (secondary aggregates) are expected to get dispersed in the coating process and may completely or partially reform before curing. However, as the samples are cured swiftly after coating, we expect the resulting configuration of CB to exhibit distinct features of a steady state configuration of aggregates in shear flow and this is what we simulate.

For simplicity, we assume that the primary function of the polymer matrix is mediating the momentum transfer between individual aggregates. Thus, we neglect the microscopic structure of the polymer in favor of including hydrodynamic interactions between carbon black aggregates.

The DLA aggregates, though isotropically generated, are far from perfectly spherical. The gyration tensor (see Appendix E1) can be used to assign an inertia ellipsoid to any rigid body. Its three eigenvectors describe the axes of the aggregate, which we label "long", "middle", and "short" axis. With the largest and smallest eigenvalues, λ_1^2 and λ_3^2, we define the effective aspect ratio of an aggregate as λ_1/λ_3 . The aspect ratio provides a simple quantity to estimate how strongly the distribution of primary particles deviates from spherical symmetry. As more primary particles are added to an aggregate, the influence of fluctuations in the growth process diminishes in comparison to the aggregate size and the average aspect ratio decreases with N. For our proof-of-principle simulations, we choose a uniform $N = 20$ for which aggregates have an average aspect ratio of roughly 3. In reality, the size of CB aggregates will be broadly distributed with a larger average

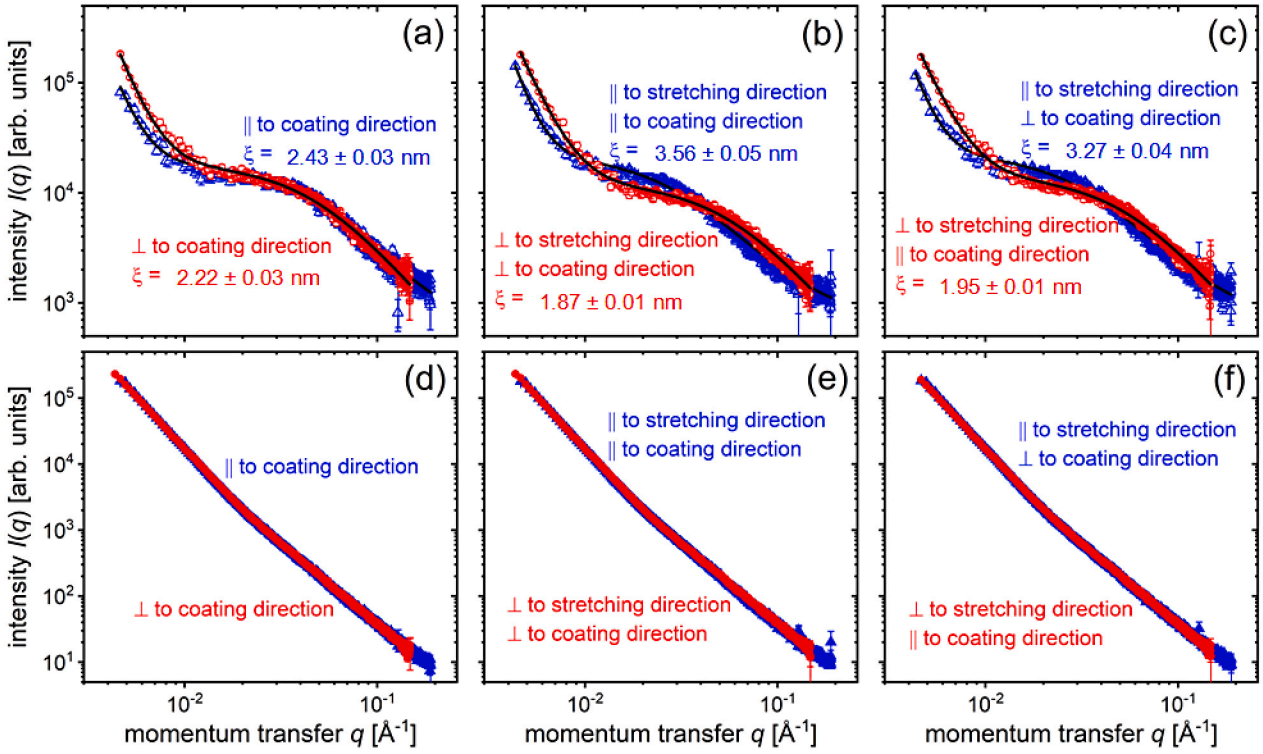

Fig. 7. One-dimensional SAXS patterns of unloaded silicone films (a, b, c) and silicone films loaded with 9 vol% CB (d, e, f) (h_{gap} = 350 µm, v_{blade} = 20 mm/s) in their unstretched state (a, d), stretched at 40% uniaxial strain parallel to the coating direction (b, e) and perpendicular to the coating direction (c, f). The patterns are evaluated in the directions as indicated in the graphs, detailed in the experimental section. The black lines are fits according to Eq. (5).

aggregate size. However, smaller aggregates are easier to simulate, and we expect any effects linked to the microscopic anisotropy of aggregates to be relatively more pronounced for smaller aggregates. For the same reason we choose a range of CB densities close to the percolation threshold.

3.4.1. *Aggregate alignment*

Just like in the experimental setup illustrated in Fig. 1, the shear flow admits three distinguished directions, i.e., flow, velocity gradient, and vorticity direction, respectively. In order to quantify whether the aggregate axes adopt a preferential orientation under shear, we can define the nematic order parameter

$$S = \left\langle \frac{3\cos^2(\theta) - 1}{2} \right\rangle , \tag{8}$$

with θ denoting the angle between one of the principal axes of an aggregate and the direction of the shear flow. As a more nuanced indicator of anisotropy, we also depict the relative frequencies of the orientation of each axis as a histogram using a Mollweide projection.

We simulated ensembles of aggregates in shear flow with Lees-Edwards boundary conditions using molecular dynamics (MD) with Multi-Particle Collision (MPC) dynamics [63–70] and a strict profile-biased thermostat. MPC dynamics is a particle-based Navier Stokes solver, providing hydrodynamic interactions and thermal fluctuations using a mesoscale solvent that can be coupled to standard MD simulations (cf. Appendix E for details).

To quantify the strength of the shear flow, we introduce the Péclet number as $Pe = \dot{\gamma} R_g^2 / D$, with the shear rate $\dot{\gamma}$, the radius of gyration R_g and the center of mass diffusion coefficient D of the aggregates. The diffusion constant can be measured via the aggregate mean squared displacement in equilibrium simulations but it is difficult to assess D experimentally. However, it is reasonable to assume that advective forces dominate the coating process and Péclet numbers will be correspondingly large. More concretely, we can roughly estimate the effective diffusion constant in the experiment. The viscosity of the quiescent material is in the order of 10^4 Pa s [28]. For such a viscous fluid, we can estimate the diffusion constant through a Stokes-Einstein relation, with $R_g \approx 100$ nm serving as the relevant length scale. With the experimental shear rates varying between $10^1\ s^{-1}$ and $10^3\ s^{-1}$ we obtain Péclet numbers of order $10^6 - 10^8$. This is strong shear, in fact too strong to be simulated straightforwardly as we run into numerical instabilities for $Pe \gg 10^3$. Yet, the purpose of the Péclet number is to identify the relevant mechanism which in our case is clearly advection, i.e., in order to compare with the experiment we need to focus on the high Péclet regime. As we shall see below, the relevant observables in that regime are largely independent of Pe, justifying our usage of slightly lower Péclet numbers.

To assess whether CB aggregates align under shear, we conducted MPC-MD simulations for a broad range of Péclet numbers. The alignment of the three aggregate axes is measured by calculating the nematic order parameters with respect to the flow, velocity gradient, and vorticity axes, respectively, for increasing Péclet numbers. The results are illustrated in Fig. 8.

For $Pe = 2.3$, where shear and diffusion have similar influence, and at lower shear rates, there is no discernible signature of alignment. However, starting from $Pe = 5.8$, the particles tend to align their long axis in the direction of flow. The negative order parameter in the gradient direction signifies that the long axes of the aggregates are preferentially orthogonal to the gradient. In combination with the vanishing nematic order parameter in vorticity direction, the overall picture indicates that aggregates tend to orient in the vorticity-flow plane. This is supported by the nematic order parameters of the short axis, which frequently aligns parallel to the gradient and perpendicular to the flow direction. However, the magnitude of all order parameters underlines that the overall alignment is weak compared to a nematic phase.

To improve the visualization of this alignment, we use Mollweide projections of the aggregate axes in spherical coordinates (Fig. 9). The

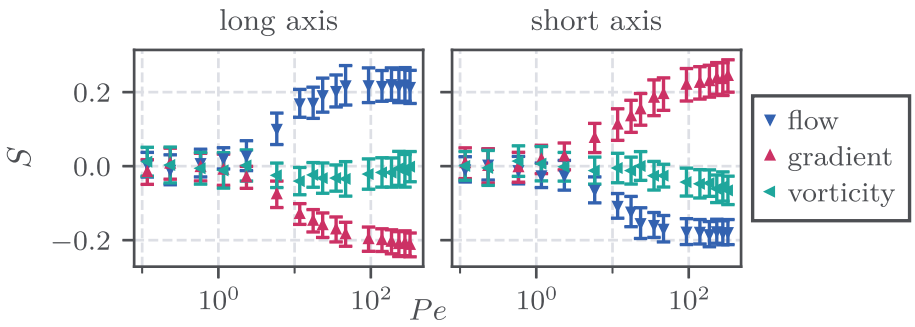

Fig. 8. Nematic order parameters of the long and short axes of aggregates with respect to the flow, gradient and vorticity axes for increasing Péclet number. CB number density was 6.7%. Error bars encode the standard deviation.

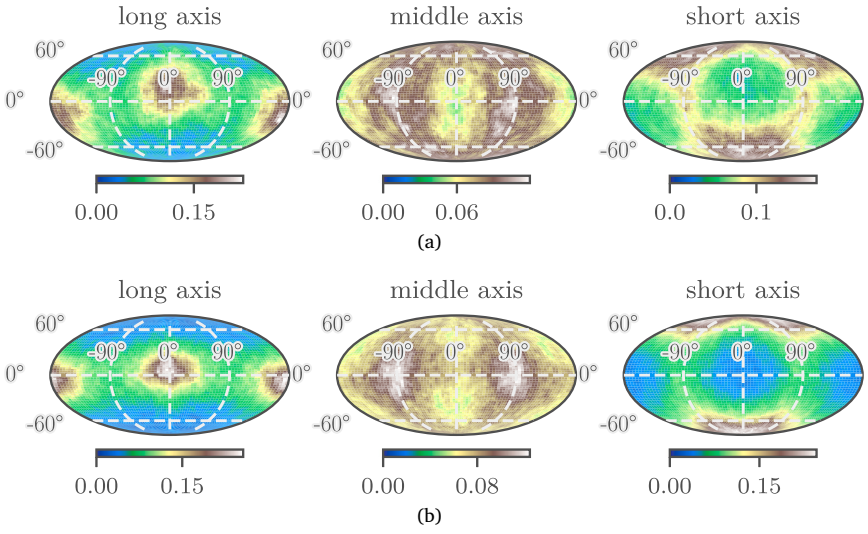

Fig. 9. Mollweide projections of the distributions of the orientation of aggregate axes for weak ($Pe = 11.7$, top) and strong flow ($Pe = 93.4$, bottom), respectively.

polar angle θ corresponds to the gradient direction and is chosen such that the poles are represented by $\theta = \pm 90°$. The azimuthal angle ϕ is measured with respect to the flow-gradient plane and thus encodes the vorticity direction at $(\phi, \theta) = (\pm 90°, 0°)$ (see Appendix E3 for more details).

Fig. 9 displays the distributions of the aggregate axes. It corroborates that the long axes of aggregates preferentially point in the flow direction and lie in the flow-vorticity plane. The short axis is parallel to the gradient direction, i.e., at the poles of the projection. The behavior of the middle axis is less clear, yet a maximum can be identified that is related to a slight alignment with the vorticity axis. The features of the distributions become more pronounced with increasing shear rate. There is also evidence of a break in symmetry with respect to the polar angle. For example, the maxima of the distribution of the long axis are shifted away from the $\theta = 0°$ circle of latitude corresponding to the flow direction. This indicates that long axes are preferentially at a slight angle with respect to the flow-vorticity plane towards the gradient direction, as known experimentally [71] and theoretically [72] for rods, an effect that is reduced for stronger flows.

Thus, we can conclude that aggregates show alignment in shear flow, exhibiting behavior similar to the phenomenology previously observed for aggregates fracturing in shear flow [73] as well as for rod-like particles [74–77]. Yet, the alignment effect, even in strong flow, is weak with nematic order parameters around 0.2, largely insensitive to the shear rate. The microscopic randomness of the aggregates and their three distinct principal axes do not appear to have a strong effect, since the observed phenomenology resembles the one of much simpler elongated particles like ellipsoids [78].

Our findings contrast the experimental characterizations which showed no indication of aggregate alignment with the flow direction in spite of large Péclet numbers. Note, however, that the simulated alignment is small and the "long" axis of an aggregate is difficult to be discerned from a planar picture. Anisometry may be present but difficult to detect experimentally. In the following, we thus use the experimentally measured electrical anisotropy as a probe for anisometric structure and provide a model to interpret it structurally.

3.4.2. *Anisotropic conductivity*

A macroscopically conductive CB composite relies on a percolating network of CB aggregates. We can infer these networks from our simulations by assigning a threshold distance d effectively describing a cutoff distance for tunneling transport. Treating the remaining tunneling links as a random resistor network and introducing two electrodes connected to two opposite sides of the simulation box we can quantify the conductivity of the composite following Ref. [79]. A detailed description can be found in appendix E5.

As the MPC simulations are computationally demanding and probably do not generate the experimental flow characteristics, we switch to equilibrium Monte Carlo simulations with an external alignment potential

$$V_A(\boldsymbol{\omega}) = -A(\boldsymbol{\omega} \cdot \boldsymbol{e}_z)^2 \,, \tag{9}$$

with the orientation of the long axis of an aggregate denoted as ω and the field strength A. These simplified simulations do not accurately reproduce the aggregate orientations observed in shear flow but we

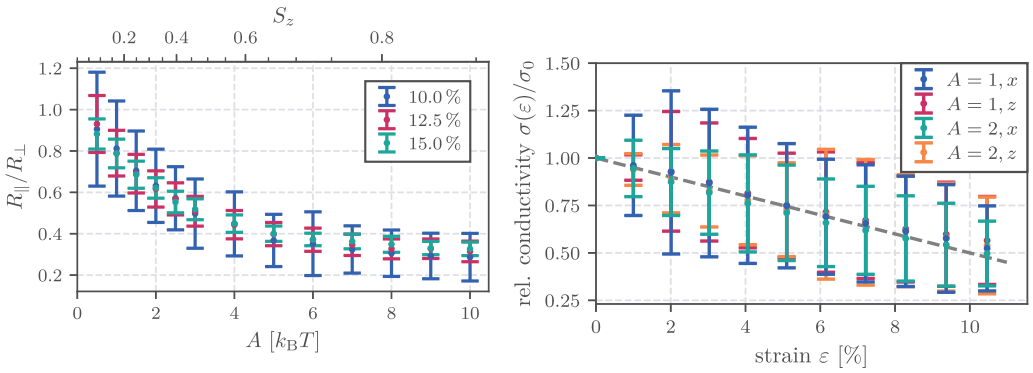

Fig. 10. Left: Electrical anisotropy ratio induced by an external alignment field with amplitude A for different filler densities. Points mark the mean ratio averaged over 100 networks and error bars show the corresponding standard variation. The nematic order parameter S_z is a monotonic function of A (unaltered across the three densities) and is depicted as the non-linear top axis. Right: Simulated tensile test. Affine deformation reduces conductivity but is insensitive to alignment direction and strength. The gray dotted line indicates the common linear decay.

can control the orientation of the long axis to probe the relationship between microscopic alignment of aggregates and conductivity. As we have access to much larger system sizes and a higher number of independent snapshots to work with, our observations bear higher statistical significance.

Fig. 10 illustrates the results of our composite conductivity measurements. For all field strengths, the average electric anisotropy ratio is smaller than one, indicating that conductivity is robustly enhanced in the direction of preferential alignment. The effect becomes more pronounced as the field strength is increased, inducing stronger alignment as measured by the nematic order parameter S_z of the long axis relative to the alignment direction. An amplitude of $A = 1.5\,k_BT$ roughly reproduces the S_z order parameter of the MPC-MD simulations for large Péclet numbers. The absolute resistivities are subject to strong fluctuations and so is the ratio $R_\parallel/R_\perp$, with individual networks exhibiting ratios larger than one. These fluctuations diminish with A as well as the density. As the density of 10% is just above the percolation threshold without external alignment, the networks, particularly for weak alignment, have few redundancies. Thus, they depend on specific links that on breakage cause strong conductivity fluctuations. This effect is amplified by the finite size of the simulation. At larger densities, networks have more connections, reducing the impact of individual links.

The trend observed in simulations is again similar to previous studies on rod-like particles. We observe electrical anisotropy due to microscopic alignment. The experiments report an electric anisotropy ratio larger than 1 for unstrained films. Thus, if aggregate alignment is the relevant mechanism, the alignment axis would have to be closer to the vorticity axis rather than the direction of flow. Yet, this would imply that simple shear flow is insufficient to describe the coating process. This supports the conclusion drawn in Section 3.1.

3.4.3. Piezoresistivity

We simulated uniaxial tensile strain naively by applying an affine transformation to the centers of mass of all aggregates while preserving the rigid structure and the orientation of individual aggregates. This is the simplest elasticity model and neglects the polymer structure in favor of an elastic continuum, but should suffice for small strains ε. We preserve the volume of the simulation box corresponding to a Poisson ratio of 0.5, commensurate for rubbers. In order to amplify potential anisotropies we simulated right above the percolation threshold and calculated the conductivity for stretched configurations to examine anisotropic piezoresistivity.

Fig. 10 illustrates that the average change in conductivity induced by strain $\sigma(\varepsilon)$ relative to the unstrained conductivity σ_0 is entirely insensitive to the aggregate alignment. Conductivity decays in excellent approximation linearly with the strain featuring a common decay rate of roughly 5% per %-strain. Thus, 10% strain double the resistivity which agrees well with the experimental tensile test in coating direction. The electric anisotropy ratio remains constant throughout the deformation. At larger strain, saturation effects emerge as the aggregates collide due to compression perpendicular to the strain direction.

3.5. Structural model for the observed electric anisotropy

The immediate structural observations of SAXS and nanomechanical mapping did not indicate microscopic alignment of aggregates or agglomerates in the direction of flow. The conductivity measurements on unstrained samples indicated an electric anisotropy ratio $\kappa > 1$, while our conductivity simulations predict that alignment with flow leads to $\kappa < 1$. Thus, direct and indirect evidence suggest that there is no discernable aggregate alignment in flow direction. This markedly differs from our hydrodynamic simulations as well as previous experimental [6,35,36,51] and computational [73–77] studies on elastomers featuring rodlike fillers.

We hypothesize that the CB distribution generated by doctor blade coating is not adequately described by simple shear flow in steady state. We find that CB is well dispersed in the silicone matrix in the composites, suggesting that preexisting filler networks are fragmented into primary aggregates during coating, indicative of shear-thinning. It seems likely that the flow induced by the coating contains extensional components in the direction of the flow. The resultant larger inter-aggregate distances increases resistance in coating direction similar to the simulated effect of tensile strain.

This assumption alone does not explain the flip of the piezoelectric anisotropy ratio when external strain is applied. The only strain-induced structural change that we could observe directly is a slight shift towards higher circularity and smaller particle diameters in the nanomechanical mapping. As it is unlikely that primary aggregates break under shear, it appears that either agglomerates are increasingly dispersed, or aggregates change their orientation. If aggregates were isotopically oriented, the spreading of agglomerates should increase resistance independent of strain direction. Thus, we suspect that aggregate alignment changes reversibly during strain, inducing the observed anisotropic piezoresistivity.

The SAXS results exclude preferential alignment with flow or vorticity direction. However, nanomechanical mapping finds a non-uniform distribution of Feret angles in the flow-vorticity plane. The Feret angles only indirectly resolve aggregate orientation but for isotropic agglomerates, any two-dimensional projection should result in a uniform distribution of Feret angles. The anisometry appears to be the product of extensional flow components due to non-linear rheology of the polymer-CB mixture. It is, surprisingly, sufficient to cause some electrical and comparably strong piezoresistive anisotropy.

4. Conclusions

We report on flow-induced (piezo-)electric anisotropy of CB elastomers relevant for sensing applications and the underlying structure–property relationships. The results help understand and emphasize the impact of processing on the macroscopic properties of elastomers thus outlining paths to tune and optimize those properties by adjusting the fabrication process.

Doctor blade coating liquid CB-silicone mixtures with CB concentrations above the percolation threshold (7/9/11 vol%) led to slight electrical and strong piezoresistive anisotropy in cured films. Conductivities and piezoresistive sensitivities were higher perpendicular to the coating direction than parallel to it for all examined compositions, gap heights and shear rates. In contrast, the mechanical anisotropies were always negligible. Electrical conductivity in CB-silicone films necessitates percolation, while the mechanical reinforcement of CB does not. Piezoresistive sensitivity and its anisotropy increased upon approaching the percolation threshold.

Molecular dynamics simulations of atomistic CB agglomerates suggest that shear flow induces weak preferential alignment on the aggregate level. This in turn causes higher conductivity in coating direction as fewer tunneling contacts suffice to traverse the simulation box. We can attribute this anisotropy to the geometry of the contact network. Tensile strain reduces conductivity in all directions preserving the anisotropy ratio of the unstrained state. This effect is consistent with the existence of larger separations between aggregates on the shortest path partially compensated by additional routes exploring perpendicular directions.

We propose that in unstrained films, increased interparticle distances parallel to the coating direction as a result of extensional flow are the dominant mechanism to cause the experimental observation $R_{\parallel}/R_{\perp} > 1$. In contrast, subtle changes of aggregate orientations in the flow-vorticity plane become relevant when the samples are strained. This causes resistances to increase more strongly when strained perpendicular to the coating direction.

It should be possible in the future to directly observe such processes using *in situ* SAXS approaches that have already been applied e.g. to observe the alignment of graphite flakes during slot die coating [80]. Systematic variations in slit geometry and velocity and rheological tuning of the paste could directly reveal the role of extensional flow. As an alternative, extrusion from a nozzle in the X-ray beam [81] may provide more direct data, albeit further removed from the true production geometry.

In conclusion, flow-induced structural anisotropy in CB-silicone composites may be hard to detect but can cause strong piezoelectric anisotropy. Since mechanical anisotropy is negligible, we have further shown that mechanical and electrical anisotropy are largely independent. Our results indicate that the common picture on the impact of directional flow on anisometric particles in liquid polymeric matrices, i.e., preferential alignment in the flow direction, is too simplistic in the case of our CB-silicone composites.

CRediT authorship contribution statement

Bettina Zimmer: Writing – review & editing, Writing – original draft, Visualization, Validation, Methodology, Investigation, Formal analysis, Data curation, Conceptualization. **Bart-Jan Niebuur:** Writing – review & editing, Writing – original draft, Investigation, Formal analysis, Data curation. **Florian Schaefer:** Writing – review & editing, Writing – original draft, Methodology, Investigation. **Fabian Coupette:** Writing – review & editing, Writing – original draft, Methodology, Investigation. **Victor Tänzel:** Writing – review & editing, Writing – original draft, Methodology, Investigation. **Tanja Schilling:** Writing – review & editing, Validation, Supervision, Resources, Project administration, Investigation, Funding acquisition, Conceptualization. **Tobias Kraus:** Writing – review & editing, Validation, Supervision, Resources, Project administration, Methodology, Investigation, Funding acquisition, Conceptualization.

Declaration of competing interest

The authors declare the following financial interests/personal relationships which may be considered as potential competing interests: Tobias Kraus reports financial support was provided by German Research Foundation. If there are other authors, they declare that they have no known competing financial interests or personal relationships that could have appeared to influence the work reported in this paper.

Acknowledgments

We thank Werner Schneider and Herbert Beermann for manufacturing the four-point probe setup, Lola González-García and Dominik Schmidt for helpful discussions. The authors gratefully acknowledge the Core Facility for Correlative Microscopy and Tomography (CoMiTo) at Saarland University for providing access to the AFM used for PeakForce QNM measurements, and the German Research Foundation (DFG) for funding the AFM instrument (INST 256/455-1 FUGG). Furthermore, we are grateful to Marisol Ripoll and Roland Winkler for helpful discussions regarding MPC. Funded by the Deutsche Forschungsgemeinschaft (DFG, German Research Foundation), Germany under Germany's Excellence Strategy – EXC-2193/1 – 390951807. Funded by the Deutsche Forschungsgemeinschaft (DFG, German Research Foundation), Germany - 404913146, 457534544, 531007218. The authors acknowledge support by the state of Baden-Württemberg through bwHPC and the German Research Foundation (DFG) through grant no INST 39/963-1 FUGG (bwForCluster NEMO).

Appendix A. Supplementary data

Supplementary material related to this article can be found online at https://doi.org/10.1016/j.cartre.2026.100623.

Data availability

Data will be made available on request.

References

[1] S. Araby, Q. Meng, L. Zhang, I. Zaman, P. Majewski, J. Ma, Elastomeric composites based on carbon nanomaterials, Nanotechnology 26 (11) (2015).
[2] L. Flandin, A. Chang, S. Nazarenko, A. Hiltner, E. Baer, Effect of strain on the properties of an ethylene-octene elastomer with conductive carbon fillers, J. Appl. Polym. Sci. 76 (6) (2000) 894–905.
[3] C.B. Karuthedath, U. Fikri, F. Ruf, N. Schwesinger, Characterization of carbon black filled PDMS-composite membranes for sensor applications, Key Eng. Mater. 753 (2017) 18–27.
[4] J. Kost, M. Narkis, A. Foux, Effects of axial stretching on the resistivity of carbon black filled silicone rubber, Polym. Eng. Sci. 23 (10) (1983) 567–571.
[5] Y. Li, X. Huang, L. Zeng, R. Li, H. Tian, X. Fu, Y. Wang, W.-H. Zhong, A review of the electrical and mechanical properties of carbon nanofiller-reinforced polymer composites, J. Mater. Sci. 54 (2019) 1036–1076.
[6] I. Balberg, N. Binenbaum, S. Bozowski, Anisotropic percolation in carbon black-polyvinylchloride composites, Solid State Commun. 47 (12) (1983) 989–992.
[7] J.-C. Huang, Carbon black filled conducting polymers and polymer blends, Adv. Polym. Technol. 21 (4) (2002) 299–313.
[8] J. Kost, M. Narkis, A. Foux, Resistivity behavior of carbon-black-filled silicone rubber in cyclic loading experiments, J. Appl. Polym. Sci. 29 (12) (1984) 3937–3946.
[9] M. Okano, M. Fujii, S. Watanabe, Anisotropic percolation conduction in elastomer-carbon black composites investigated by polarization-sensitive terahertz time-domain spectroscopy, Appl. Phys. Lett. 111 (2017).
[10] M. Knite, V. Teteris, A. Kiploka, J. Kaupuzs, Polyisoprene-carbon black nanocomposites as tensile strain and pressure sensor materials, Sensors Actuators A 110 (1–3) (2004) 142–149.
[11] M. Knite, V. Teteris, A. Kiploka, I. Klemenoks, Reversible tenso-resistance and piezo-resistance effects in conductive polymer-carbon nanocomposites, Adv. Eng. Mater. 6 (9) (2004) 742–746.

[12] M. Panahi-Sarmad, M. Noroozi, M. Abrisham, S. Eghbalinia, F. Teimoury, A.R. Bahramian, P. Dehghan, M. Sadri, V. Goodarzi, A comprehensive review on carbon-based polymer nanocomposite foams as electromagnetic interference shields and piezoresistive sensors, ACS Appl. Electron. Mater. 2 (2020) 2318–2350.
[13] X. Wang, X. Liu, D.W. Schubert, Highly sensitive ultrathin flexible thermoplastic polyurethane/carbon black fibrous film strain sensor with adjustable scaffold networks, Nano-Micro Lett. 13 (64) (2021).
[14] J. Zavickis, M. Knite, G. Podins, A. Linarts, R. Orlovs, Polyisoprene-nanostructured carbon composite – a soft alternative for pressure sensor application, Sensors Actuators A 171 (1) (2011) 38–42.
[15] C. Cattin, P. Hubert, Piezoresistance in polymer nanocomposites with high aspect ratio particles, ACS Appl. Mater. Interfaces 6 (3) (2014) 1804–1811.
[16] S. Chen, R. Wu, P. Li, Q. Li, Y. Gao, B. Qian, F. Xuan, Acid-interface engineering of carbon nanotube/elastomers with enhanced sensitivity for stretchable strain sensors, ACS Appl. Mater. Interfaces 10 (43) (2018) 37760–37766.
[17] M. Nankali, N.M. Nouri, M. Navidbakhsh, N.G. Malek, M.A. Amindehghan, A.M. Shahtoori, M. Karimi, M. Amjadi, Highly stretchable and sensitive strain sensors based on carbon nanotube–elastomer nanocomposites: the effect of environmental factors on strain sensing performance, J. Mater. Chem. C 8 (18) (2020) 6185–6195.
[18] J. Chen, J. Zheng, Q. Gao, J. Zhang, J. Zhang, O.M. Omisore, L. Wang, H. Li, Polydimethylsiloxane (PDMS)-based flexible resistive strain sensors for wearable applications, Appl. Sci. 8 (3) (2018) 345.
[19] G. Shi, Z. Zhao, J.-H. Pai, I. Lee, L. Zhang, C. Stevenson, K. Ishara, R. Zhang, H. Zhu, J. Ma, Highly sensitive, wearable, durable strain sensors and stretchable conductors using graphene/silicon rubber composites, Adv. Funct. Mater. 26 (42) (2016) 7614–7625.
[20] P. Feng, H. Ji, L. Zhang, X. Luo, X. Leng, P. He, H. Feng, J. Zhang, X. Ma, W. Zhao, Highly stretchable patternable conductive circuits and wearable strain sensors based on polydimethylsiloxane and silver nanoparticles, Nanotechnology 30 (18) (2019) 185501.
[21] J. Lee, S. Kim, J. Lee, D. Yang, B.C. Park, S. Ryu, I. Park, A stretchable strain sensor based on a metal nanoparticle thin film for human motion detection, Nanoscale 6 (20) (2014) 11932–11939.
[22] S.-J. Park, M.-K. Seo, C. Nah, Influence of surface characteristics of carbon blacks on cure and mechanical behaviors of rubber matrix compoundings, J. Colloid Interface Sci. 291 (2005) 229–235.
[23] P. Datta, R. Friel, Surface treatment of conductive carbon blacks and their effect on the properties of conductive composites, in: H. Ishida, G. Kumar (Eds.), Molecular Characterization of Composite Interfaces, Springer, Berlin, Heidelberg, 1985.
[24] M.E. Spahr, R. Rothon, Carbon black as a polymer filler, in: S. Palsule (Ed.), Polymers and Polymeric Composites: A Reference Series, Springer, Berlin, Heidelberg, 2016.
[25] F. Coupette, L. Zhang, B. Kuttich, A. Chumakov, S.V. Roth, L. González-García, T. Kraus, T. Schilling, Percolation of rigid fractal carbon black aggregates, J. Chem. Phys. 155 (12) (2021) 124902.
[26] L. Flandin, T. Prasse, R. Schueler, K. Schulte, W. Bauhofer, J.-Y. Cavaille, Anomalous percolation transition in carbon-black-epoxy composite materials, Phys. Rev. B 59 (22) (1999) 14349–14355.
[27] K. Miyasaka, K. Watanabe, E. Jojima, H. Aida, M. Sumimta, K. Ishikawa, Electrical conductivity of carbon-polymer composites as a function of carbon content, J. Mater. Sci. 17 (1982) 1610–1616.
[28] L. Zhang, D.S. Schmidt, L. González-García, T. Kraus, Microscopic softening mechanisms of an ionic liquid additive in an electrically conductive carbon-silicone composite, Adv. Mater. Technol. 7 (11) (2022).
[29] M. Abdul Sattar, Surface activated pyrolytic carbon black: A dual functional sustainable filler for natural rubber composites, ChemSusChem 17 (2) (2024) 1–11.
[30] M. Knite, V. Teteris, A. Kiploka, The effect of plasticizing agent on strain-induced change of electric resistivity of carbon–polyisoprene nano-composites, Mater. Sci. Eng.: C 23 (6–8) (2003) 787–790.
[31] S.-P. Rwei, F.-H. Ku, K.-C. Cheng, Dispersion of carbon black in a continuous phase: Electrical, rheological, and morphological studies, Colloid Polym. Sci. 280 (12) (2002) 1110–1115.
[32] F. Ehrburger-Dolle, M. Hindermann-Bischoff, E. Geissler, C. Rochas, F. Bley, F. Livet, Role of fractal features in the structure-property relationships of carbon black filled polymers, MRS Proc. 661 (2011) KK7.4.
[33] M. Huang, L.B. Tunnicliffe, J. Zhuang, W. Ren, H. Yan, J.J. Busfield, Strain-dependent dielectric behavior of carbon black reinforced natural rubber, Macromolecules 49 (6) (2016) 2339–2347.
[34] M. Leboeuf, N. Ghamri, B. Brulé, T. Coupez, B. Vergnes, Influence of mixing conditions on rheological behavior and electrical conductivity of polyamides filled with carbon black, Rheol. Acta 47 (2008) 201–212.
[35] E. Vigueras-Santiago, S. Hernández-López, M.A. Camacho-López, O. Lara-Sanjuan, Electric anisotropy in high density polyethylene + carbon black composites induced by mechanical deformation, J. Phys.: Conf. Ser. 167 (012039) (2009).
[36] Y.-C. Zhang, K. Dai, J.-H. Tang, X. Ji, Z.-M. Li, Anisotropically conductive polymer composites with a selective distribution of carbon black in an in situ microfibrillar reinforced blend, Mater. Lett. 64 (2010) 1430–1432.
[37] F. Ehrburger-Dolle, M. Hindermann-Bischoff, F. Livet, F. Bley, C. Rochas, E. Geissler, Anisotropic ultra-small-angle X-ray scattering in carbon black filled polymers, Langmuir 17 (2) (2001) 329–334.
[38] V. Grenard, N. Taberlet, S. Manneville, Shear-induced structuration of confined carbon black gels: steady-state features of vorticity-aligned flocs, Soft Matter 7 (2011) 3920–3928.
[39] A.S. Negi, C.O. Osuji, New insights on fumed colloidal rheology—shear thickening and vorticity-aligned structures in flocculating dispersions, Rheol. Acta 48 (2009) 871–881.
[40] C.O. Osuji, C. Kim, D.A. Weitz, Shear thickening and scaling of the elastic modulus in a fractal colloidal system with attractive interactions, Phys. Rev. E 77 (060402) (2008).
[41] C.O. Osuji, D.A. Weitz, Highly anisotropic vorticity aligned structures in a shear thickening attractive colloidal system, Soft Matter 4 (2008) 1388–1392.
[42] I. Miccoli, F. Edler, H. Pfnür, C. Tegenkamp, The 100th anniversary of the four-point probe technique: the role of probe geometries in isotropic and anisotropic systems, J. Phys.: Condens. Matter. 27 (223201) (2015).
[43] Y. Hua, PeakForce-QNM Advanced Applications Training 2014, report, Bruker, 2014.
[44] B. Pittenger, Nanoscale Mechanical Property Measurements in AFM Modes with Direct Force Control. Part I: Peakforce Tapping and Force Volume Mechanical Property Mapping, Report, Bruker, 2014.
[45] B. Pittenger, N. Erina, C. Su, Quantitative Mechanical Property Mapping at the Nanoscale With PeakForce QNM, Report, Bruker, 2010.
[46] C.A. Schneider, W.S. Rasband, K.W. Eliceiri, NIH image to imagej: 25 years of image analysis, Nature Methods 9 (7) (2012) 671–675.
[47] J. Schindelin, I. Arganda-Carreras, E. Frise, V. Kaynig, M. Longair, T. Pietzsch, S. Preibisch, C. Rueden, S. Saalfeld, B. Schmid, et al., Fiji: an open-source platform for biological-image analysis, Nature Methods 9 (7) (2012) 676–682.
[48] J. Ohser, F. Mücklich, Statistical Analysis of Microstructures in Materials Science, John Wiley & Sons, 2000.
[49] E. Geissler, F. Horkay, A.-M. Hecht, C. Rochas, P. Lindner, C. Bourgaux, G. Couarazze, Investigation of PDMS gels and solutions by small angle scattering, Polymer 38 (1) (1997) 15–20.
[50] K. Urayama, T. Kawamura, Y. Hirata, S. Kohjiya, SAXS study on poly(dimethylsiloxane) networks with controlled distributions of chain lengths between crosslinks, Polymer 39 (16) (1998) 3827–3833.
[51] Y. Sohn, D. Kim, S.-H. Partk, S.-E. Lee, Seamless tube-type heater with uniform thickness and temperature distribution based on carbon nanotubes aligned by circumferential shearing, Materials 12 (20) (2019).
[52] J.B. Hipp, Structure, Rheology, and Electrical Conductivity of High-Structured Carbon Black Suspensions (Ph.D. thesis), University of Delaware, 2020.
[53] V. Grenard, N. Taberlet, S. Manneville, Direct measurements of the microstructural origin of shear-thinning in carbon black suspensions, J. Rheol. 65 (145) (2021) 145–157.
[54] J.J. Richards, P.Z. Ramos, Q. Liu, A review of the shear rheology of carbon black suspensions, Front. Phys. 11 (2023) 1–11.
[55] L. Mullins, Softening of rubber by deformation, Rubber Chem. Technol. 42 (1969) 339–362.
[56] K. Yamaguchi, J.J.C. Busfield, A.G. Thomas, Electrical and mechanical behavior of filled elastomers. I. The effect of strain, J. Polym. Sci. B 41 (17) (2003) 2079–2089.
[57] M. Knite, V. Teteris, B. Polyakov, D. Erts, Electric and elastic properties of conductive polymeric nanocomposites on macro- and nanoscales, Mater. Sci. Eng.: C 19 (1–2) (2002) 15–19.
[58] F. Carmona, A. El Amarti, Anisotropic electrical conductivity in heterogeneous solids with cylindrical conducting inclusions, Phys. Rev. B 35 (7) (1987) 3284–3290.
[59] C. Tian, J. Cui, L. Zhang, M. Tian, Quantitative characterization of interfacial properties of carbon black/elastomer nanocomposites and mechanism exploration on their interfacial interaction, Compos. Sci. Technol. 222 (109367) (2022).
[60] A. Wonisch, P. Polfer, T. Kraft, A. Dellert, A. Heunisch, A. Roosen, A comprehensive simulation scheme for tape casting: from flow behavior to anisotropy development, J. Am. Ceram. Soc. 94 (7) (2011) 2053–2060.
[61] L.J. Lanticse, Y. Tanabe, K. Matsui, Y. Kaburagi, K. Suda, M. Hoteida, M. Endo, E. Yasuda, Shear-induced preferential alignment of carbon nanotubes resulted in anisotropic electrical conductivity of polymer composites, Carbon 44 (14) (2006) 3078–3086.
[62] M. Klüppel, G. Heinrich, Fractal structures in carbon black reinforced rubbers, Rubber Chem. Technol. 68 (4) (1995) 623–651.
[63] A. Malevanets, R. Kapral, Mesoscopic model for solvent dynamics, J. Chem. Phys. 110 (17) (1999) 8605–8613.
[64] G. Gompper, T. Ihle, D. Kroll, R. Winkler, Multi-particle collision dynamics: A particle-based mesoscale simulation approach to the hydrodynamics of complex fluids, Adv. Comput. Simul. Approaches Soft Matter Sci. III (2009) 1–87.
[65] M.P. Howard, A. Nikoubashman, J.C. Palmer, Modeling hydrodynamic interactions in soft materials with multiparticle collision dynamics, Curr. Opin. Chem. Eng. 23 (2019) 34–43.
[66] R. Chen, R. Poling-Skutvik, A. Nikoubashman, M.P. Howard, J.C. Conrad, J.C. Palmer, Coupling of nanoparticle dynamics to polymer center-of-mass motion in semidilute polymer solutions, Macromolecules 51 (5) (2018) 1865–1872.

[67] A.P. Thompson, H.M. Aktulga, R. Berger, D.S. Bolintineanu, W.M. Brown, P.S. Crozier, P.J. in 't Veld, A. Kohlmeyer, S.G. Moore, T.D. Nguyen, R. Shan, M.J. Stevens, J. Tranchida, C. Trott, S.J. Plimpton, LAMMPS - a flexible simulation tool for particle-based materials modeling at the atomic, meso, and continuum scales, Comp. Phys. Comm. 271 (2022) 108171.

[68] M.K. Petersen, J.B. Lechman, S.J. Plimpton, G.S. Grest, P. Schunk, et al., Mesoscale hydrodynamics via stochastic rotation dynamics: Comparison with Lennard-Jones fluid, J. Chem. Phys. 132 (17) (2010).

[69] P.J. in't Veld, S.J. Plimpton, G.S. Grest, Accurate and efficient methods for modeling colloidal mixtures in an explicit solvent using molecular dynamics, Comput. Phys. Comm. 179 (5) (2008) 320–329.

[70] T. Shire, K.J. Hanley, K. Stratford, DEM simulations of polydisperse media: efficient contact detection applied to investigate the quasi-static limit, Comput. Part. Mech. 8 (4) (2021) 653–663.

[71] J. Vermant, H. Yang, G. Fuller, Rheooptical determination of aspect ratio and polydispersity of nonspherical particles, AIChE J. 47 (4) (2001) 790–798.

[72] R. Winkler, K. Mussawisade, M. Ripoll, G. Gompper, Rod-like colloids and polymers in shear flow: a multi-particle-collision dynamics study, J. Phys.: Condens. Matter. 16 (38) (2004) S3941.

[73] E. Asylbekov, R. Trunk, M.J. Krause, H. Nirschl, Microscale discrete element method simulation of the carbon black aggregate fracture behavior in a simple shear flow, Energy Technol. 9 (6) (2021) 2000850.

[74] S.I. White, B.A. DiDonna, M. Mu, T.C. Lubensky, K.I. Winey, Simulations and electrical conductivity of percolated networks of finite rods with various degrees of axial alignment, Phys. Rev. B 79 (2) (2009) 024301.

[75] S.S. Rahatekar, M. Hamm, M.S. Shaffer, J.A. Elliott, Mesoscale modeling of electrical percolation in fiber-filled systems, J. Chem. Phys. 123 (13) (2005).

[76] F. Shi, S. Wang, M.G. Forest, P.J. Mucha, R. Zhou, Network-based assessments of percolation-induced current distributions in sheared rod macromolecular dispersions, Multiscale Model. Simul. 12 (1) (2014) 249–264.

[77] S.P. Finner, M.I. Kotsev, M.A. Miller, P. Van Der Schoot, Continuum percolation of polydisperse rods in quadrupole fields: Theory and simulations, J. Chem. Phys. 148 (3) (2018).

[78] J.K. Dhont, W.J. Briels, Rod-like Brownian particles in shear flow, in: G. Gompper, M. Schick (Eds.), Soft Matter: Complex Colloidal Suspensions, Vol. 2, 2006.

[79] F. Dörfler, J.W. Simpson-Porco, F. Bullo, Electrical networks and algebraic graph theory: Models, properties, and applications, Proc. IEEE 106 (5) (2018) 977–1005.

[80] Y. Quan, P. He, J. Chen, N. Guo, Y. Li, H. Zheng, J. Zhang, X. Ren, Y. Zhang, W. Bao, K. Qi, G. Ding, Multi-layer shearing induced high orientation of graphene oxide sheets towards high-performance macrostructures, Carbon 226 (2024) 119179.

[81] B. Reiser, D. Gerstner, L. González-García, J.H.M. Maurer, I. Kanelidis, T. Kraus, Spinning hierarchical gold nanowire microfibers by shear alignment and intermolecular self-assembly, ACS Nano 11 (5) (2017) 4934–4942.